

NEW TWO-DIMENSIONAL MODELS OF SUPERNOVA EXPLOSIONS BY THE NEUTRINO-HEATING MECHANISM: EVIDENCE FOR DIFFERENT INSTABILITY REGIMES IN COLLAPSING STELLAR CORES

BERNHARD MÜLLER¹, HANS-THOMAS JANKA¹, AND ALEXANDER HEGER^{2,3}

Draft version August 6, 2018

ABSTRACT

The neutrino-driven explosion mechanism for core-collapse supernovae in its modern flavor relies on the additional support of hydrodynamical instabilities in achieving shock revival. Two possible candidates, convection and the so-called standing accretion shock instability (SASI), have been proposed for this role. In this paper, we discuss new successful simulations of supernova explosions that shed light on the relative importance of these two instabilities. While convection has so far been observed to grow first in self-consistent hydrodynamical models with multi-group neutrino transport, we here present the first such simulation in which the SASI grows faster while the development of convection is initially inhibited. We illustrate the features of this SASI-dominated regime using an explosion model of a $27M_{\odot}$ progenitor, which is contrasted with a convectively-dominated model of an $8.1M_{\odot}$ progenitor with subsolar metallicity, whose early post-bounce behavior is more in line with previous $11.2M_{\odot}$ and $15M_{\odot}$ explosion models. We analyze the conditions discriminating between the two different regimes, showing that a high mass-accretion rate and a short advection time-scale are conducive for strong SASI activity. We also briefly discuss some important factors for capturing the SASI-driven regime, such as general relativity, the progenitor structure, a nuclear equation of state leading to a compact proto-neutron star, and the neutrino treatment. Finally, we evaluate possible implications of our findings for 2D and 3D supernova simulations.

Subject headings: supernovae: general—hydrodynamics—instabilities—neutrinos—relativity

1. INTRODUCTION

Aspherical hydrodynamical instabilities play a paramount role in core-collapse supernovae. In the the neutrino-driven explosion mechanism in its modern guise, they are thought to be indispensable agents for enhancing the efficiency of neutrino energy deposition in the gain region sufficiently to eventually allow shock revival, but their importance does not stop there. The asphericities that already develop before the explosion is launched pre-determine the morphology of the explosion in the later phases, and are thus a crucial factor for the mixing instabilities in supernovae (Arnett et al. 1989; Kifonidis et al. 2003, 2006; Hammer et al. 2010), the development of pulsar kicks (Janka & Müller 1994; Herant 1995; Burrows & Hayes 1996; Scheck et al. 2004, 2006; Wongwathanarat et al. 2010; Nordhaus et al. 2010a, 2012), and the remnant structure (Gawryszczak et al. 2010).

In the purely hydrodynamical case (i.e. in the absence of magnetic fields), two instabilities that influence the dynamics in the supernova core in the pre-explosion phase have been identified. Already in the 1990s it was recognized that the gain layer can be unstable to convection (Bethe 1990) as the neutrino heating of the material that is advected down to the cooling region close to the proto-neutron star surface produces a negative entropy gradient. This was confirmed

by the first generation of multi-dimensional supernova models (Herant et al. 1992; Burrows & Fryxell 1992; Herant et al. 1994; Burrows et al. 1995; Janka & Müller 1996; Müller & Janka 1997). The latter indeed showed the development of violent convective overturn in the heating region and suggested that the convective exchange of strongly neutrino-heated material from close to the proto-neutron star with cool post-shock matter in combination with the longer exposure of the accreted material to neutrino heating (Buras et al. 2006a; Murphy & Burrows 2008) can provide a powerful means of increasing the efficiency of neutrino heating, boosting the post-shock pressure, and eventually reviving the stalled shock.

Another instability of a quite different nature was discovered by Blondin et al. (2003), who observed that a standing accretion shock as encountered in core-collapse supernovae may be unstable to large-scale $\ell = 1$ and $\ell = 2$ oscillation modes even in the absence of neutrino heating, a result that has been confirmed by further hydrodynamical simulations in a number of follow-up studies in 2D and 3D (Blondin & Mezzacappa 2006; Ohnishi et al. 2006; Blondin & Mezzacappa 2007; Scheck et al. 2008; Iwakami et al. 2008, 2009; Fernández & Thompson 2009b; Fernández 2010). Linear stability analyses provided a sound theoretical framework for the understanding of this “standing accretion shock instability” and identified an amplification cycle of entropy/vorticity and acoustic perturbations between the shock and the proto-neutron star surface as the underlying mechanism for the instability (Foglizzo 2002; Foglizzo et al. 2006, 2007; Yamasaki & Yamada 2007). While Blondin & Mezzacappa (2006) and Laming (2007) have argued for the possibility of a

¹ Max-Planck-Institut für Astrophysik, Karl-Schwarzschild-Str. 1, D-85748 Garching, Germany; bjmuellr@mpa-garching.mpg.de, thj@mpa-garching.mpg.de

² School of Physics and Astronomy, University of Minnesota, 116 Church Street SE, Minneapolis, MN 55455, USA

³ Monash Center for Astrophysics, School of Mathematical Sciences, Building 28, Monash University, Victoria 3800, Australia, alexander.heger@monash.edu

purely acoustic cycle, Guilet & Fogliizzo (2012) have recently given strong arguments for an advective-acoustic cycle. Similar to convection, strong SASI activity may improve the efficiency of neutrino heating by increasing the average shock radius and therefore the residence time of matter in the gain region (Scheck et al. 2008; Marek & Janka 2009).

While convection and the SASI are well understood in the linear regime, where they can be clearly differentiated, e.g. on the basis of the dominant wavenumber, which is typically higher for the convective modes, see (Fogliizzo et al. 2006) and by means of their growth behavior (monotonic vs. oscillatory). The situation is far more complicated in the non-linear regime where both instabilities can interact with convection triggering secondary shock oscillations or vice versa, and the presence of a strong $\ell = 1$ or $\ell = 2$ mode may not necessarily be indicative of the SASI. The evidence for the SASI as “main” instability from recent 2D explosion models using elaborate multi-group transport (Buras et al. 2006a; Marek & Janka 2009; Bruenn et al. 2009; Suwa et al. 2010; Müller et al. 2012) as well as from the first tentative explorations in 3D (Takiwaki et al. 2012) is therefore ambiguous: While they all show the presence of the strong $\ell = 1$ and $\ell = 2$ shock oscillations characteristic of the SASI at late times, convection appears to be the “primary” instability in the sense that it always begins to grow first a few tens of milliseconds after bounce. Convection also appears to be the “primary” instability in the 3D models of Fryer & Warren (2002) and in recent 2D and 3D simulations based on different implementations of a simple light-bulb approximation (Murphy & Burrows 2008; Fernández & Thompson 2009a; Nordhaus et al. 2010b; Hanke et al. 2011; Burrows et al. 2012; Murphy et al. 2012). The work of Hanke et al. (2011) in particular suggests that for a certain choice of parameters in such approximate descriptions may little activity of low- ℓ modes in 3D, while the inverse turbulent energy cascade may still help to excite low- ℓ modes in 2D even though convection initially grows faster than the SASI. Except for some gray transport models with fast (prescribed) proto-neutron star contraction of Scheck et al. (2008), the primary growth of convection seems to be a generic property of simulations that include neutrino heating in some simplified or elaborate fashion. The apparent weight of evidence has even led to the suggestion “that the SASI is at most a minor feature of supernova dynamics” (Burrows et al. 2012) and that neutrino-driven convection dominates in core-collapse supernovae (Murphy et al. 2012).

However, we shall demonstrate in this paper that such a conclusion is more than premature, and that under favorable conditions the SASI plays a major role for the dynamics in the supernova core. We present new simulations of (incipient) explosions for two different progenitor stars obtained with the general relativistic multi-group neutrino hydrodynamics code VERTEX-CoCoNuT. Based on these, we show the existence of a “SASI-dominated” regime distinct from a “convection-dominated” regime for the growth of hydrodynamical instabilities as a separate route towards the explosion. After briefly introducing the numerical methods and the progenitors in Section 2, we discuss the morphology of

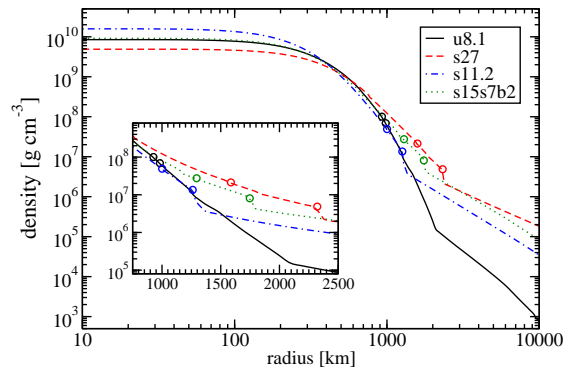


Figure 1. Density profiles for model u8.1 (black solid line) and model s27.0 (red, dashed) covering the inner 10,000 km. For comparison, profiles for the $11.2M_{\odot}$ progenitor s11.2 (blue, dash-dotted) of Woosley et al. (2002) and the $15M_{\odot}$ model s15s7b2 (green, dotted) of Woosley & Weaver (1995) are also shown. Colored circles denote the edge of the iron core and the boundary between the silicon shell and the oxygen-enriched silicon shell.

the multi-dimensional flow prior and during the incipient explosion and quantitatively analyze the growth of the SASI and convection in the different regimes in Section 3. The implications of our findings are discussed in Section 4.

2. NUMERICAL METHODS AND MODEL SETUP

We perform axisymmetric (2D) core-collapse supernova simulations with the general relativistic neutrino hydrodynamics code VERTEX-CoCoNuT (Müller et al. 2010). The hydrodynamics solver CoCoNuT is a time-explicit, directionally unsplit implementation of the piecewise parabolic method (PPM) for spherical polar coordinates using a hybrid HLLC/HLLD Riemann solver, and relies on the extended conformal flatness approximation (xCFC, Cordero-Carrión et al. 2009) for the metric equations. CoCoNuT is coupled to the neutrino transport module VERTEX (Rampp & Janka 2002), which employs a variable Eddington factor technique to solve the moment equations for the neutrino energy and momentum density with a closure provided by the formal solution of a simplified Boltzmann equation. In 2D, we resort to the “ray-by-ray-plus” approach (Buras et al. 2006b; Bruenn et al. 2006), which assumes that the neutrino distribution function is axially symmetric around the radial direction (and hence implies a radial flux vector). VERTEX includes the velocity- and metric-dependent terms as well as non-isoenergetic scattering processes, thus capturing the full complexity of multi-group transport. For the interactions between neutrinos and the matter we use an up-to-date set of opacities (see Müller et al. 2012). For details about the implementation and a discussion of the accuracy of our approach, we refer the reader to Müller et al. (2010) and Müller et al. (2012).

In this study, we consider two progenitors, namely the $27M_{\odot}$ star model s27.0 of Woosley et al. (2002) with solar metallicity, and an $8.1M_{\odot}$ model u8.1. The latter is just above the critical mass for the formation of an iron core and has an initial metallicity of approximately $Z = 10^{-4}$ (Heger et al. 2012).⁴ The structure of model u8.1 should be typical of such low-mass supernova pro-

⁴ A model of $8.0M_{\odot}$ and $Z = 10^{-4}$ did make an AGB star instead.

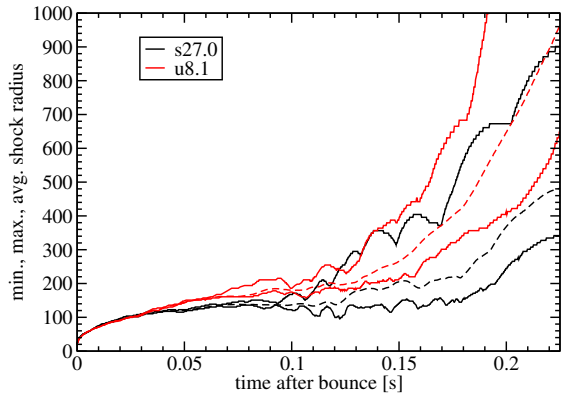


Figure 2. Maximum, minimum (solid lines) and average (dashed lines) shock radius for model s27.0 (black lines) and u8.1 (red).

genitors, and is dramatically different from stars even a few tenths of a solar mass more massive. The density profile more closely resembles an asymptotic giant branch (AGB) star, or an electron-capture supernova progenitor, than a typical massive star structure in that it has a low-density “envelope” ($\rho < 1 \text{ g cm}^{-3}$) directly on top of a dense core ($\rho > 10^6 \text{ g cm}^{-3}$) of $1.38M_{\odot}$, with a transition region of only $0.03M_{\odot}$, mostly the carbon layer, in between. Outside the $1.26M_{\odot}$ iron core are layers of silicon (out to $1.30M_{\odot}$), oxygen (to $1.36M_{\odot}$), neon, and carbon, with implosive energy generation due to silicon, oxygen, and neon burning as high as $10^{17} \text{ erg g}^{-1} \text{ s}^{-1}$. Note that the structure of model u8.1 is specific to such low-mass supernova progenitors, and not owing to the initial metallicity of the model; a different initial metallicity would only change the location and extent of the mass range between the AGB channel and the “normal” channel of iron core evolution familiar from more massive stars.

Model s27.0, by contrast, has a more massive and less compact iron core of $1.5M_{\odot}$ embedded in a thick silicon shell that reaches out to $1.68M_{\odot}$, where the transition to the oxygen-enriched silicon shell is located. Compared to model u8.1, the density drops far less rapidly outside the iron core. In order to better illustrate the different density structure of the two models, we show density profiles of the progenitors in Figure 1.

We use a numerical grid of $n_r \times n_{\theta} = 400 \times 128$ zones with non-equidistant radial spacing for both progenitors. Model s27.0 was simulated using the equation of state (EoS) of Lattimer & Swesty (1991) with a value for the bulk incompressibility modulus of nuclear matter of $K = 220 \text{ MeV}$ (LS220), while the softer variant with $K = 180 \text{ MeV}$ (LS180) was chosen for model u8.1. For a discussion of the validity of the latter EoS for small-mass (baryonic mass $\lesssim 1.5M_{\odot}$) proto-neutron stars despite its marginal inconsistency with the $1.97M_{\odot}$ neutron star found by Demorest et al. (2010), see Müller et al. (2012). Specifically, the mass-radius relation for hot and cold neutron stars is very similar for neutron stars well below the mass limit. As a consequence, both equations of state yield hardly any difference during the accretion phase (Swesty et al. 1994; Thompson et al. 2003).

3. RESULTS

Superficially, model s27.0 and u8.1 might appear to evolve in a very similar fashion: Roughly around 120 ms

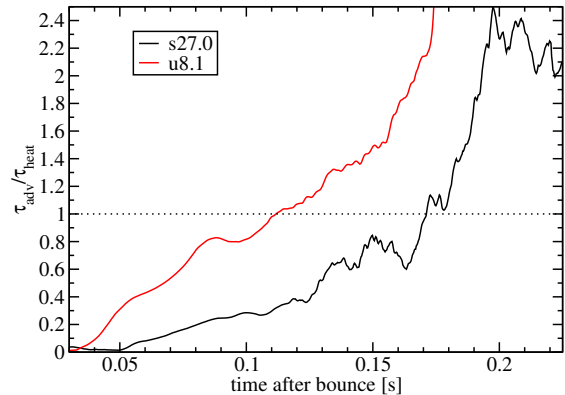


Figure 3. The runaway criterion $\tau_{\text{adv}}/\tau_{\text{heat}}$ for model s27.0 (black) and model u8.1 (red). Both τ_{adv} and τ_{heat} are evaluated as in Müller et al. (2012). Note that the curves have been smoothed using a running average over 5 ms.

after bounce the average shock radius starts to increase, and by 200 ms the shock is already expanding rapidly, although model s27.0 evidently lags behind u8.1 a little (Figure 2). Especially during the later phases, the shock becomes strongly deformed with a ratio $r_{\text{max}}/r_{\text{min}}$ of the maximum and minimum shock radius on the order of $2 \dots 3$. Both models seem to provide similar examples for an explosion at a relatively early stage.

However, this appearance is deceptive: A hint at more profound differences between s27.0 and u8.1 is already furnished by the critical ratio $\tau_{\text{adv}}/\tau_{\text{heat}}$ of the “advection” or “residence” time-scale and the heating time-scale for the material in the gain region, which serves as an indicator for an explosive runaway due to neutrino energy deposition (for $\tau_{\text{adv}}/\tau_{\text{heat}} > 1$; see Janka 2001; Thompson et al. 2005; Buras et al. 2006a; Murphy & Burrows 2008; Fernández 2012). Figure 3 shows that model s27.0 approaches the critical threshold much later than model u8.1, i.e. at roughly ~ 180 ms instead of ~ 110 ms. Nevertheless, even though the runaway condition is not yet met, the shock already expands considerably before that time in model s27.0. This suggests that at least for the first ~ 180 ms there may be a driving agent other than neutrino heating that is responsible for pushing the shock outwards. One should bear in mind, however, that it is not completely clear for which value of $\tau_{\text{adv}}/\tau_{\text{heat}}$ one could already expect a noticeable expansion of the shock: Neutrino heating might drive considerable shock expansion even for $\tau_{\text{adv}}/\tau_{\text{heat}} < 1$ depending on progenitor specifics. However, it seems inevitable that large aspherical motions in the gain regions with Mach numbers on the order of ~ 1 will affect the structure of the accretion flow, including the shock position (cp. Section 3.1).

3.1. Growth of Instabilities

The reason for the peculiar evolution of the $27M_{\odot}$ progenitor is to be sought in the strong and relatively unimpeded growth of the SASI as primary instability during the first ~ 200 ms as opposed to neutrino-driven convection in the $8.1M_{\odot}$ star – a feature hitherto not reported from full multi-group neutrino hydrodynamics simulations (Marek & Janka 2009; Müller et al. 2012).

As shown by Figures 5 and 4, the morphology of the post-shock flow in model u8.1 and model s27.0 be-

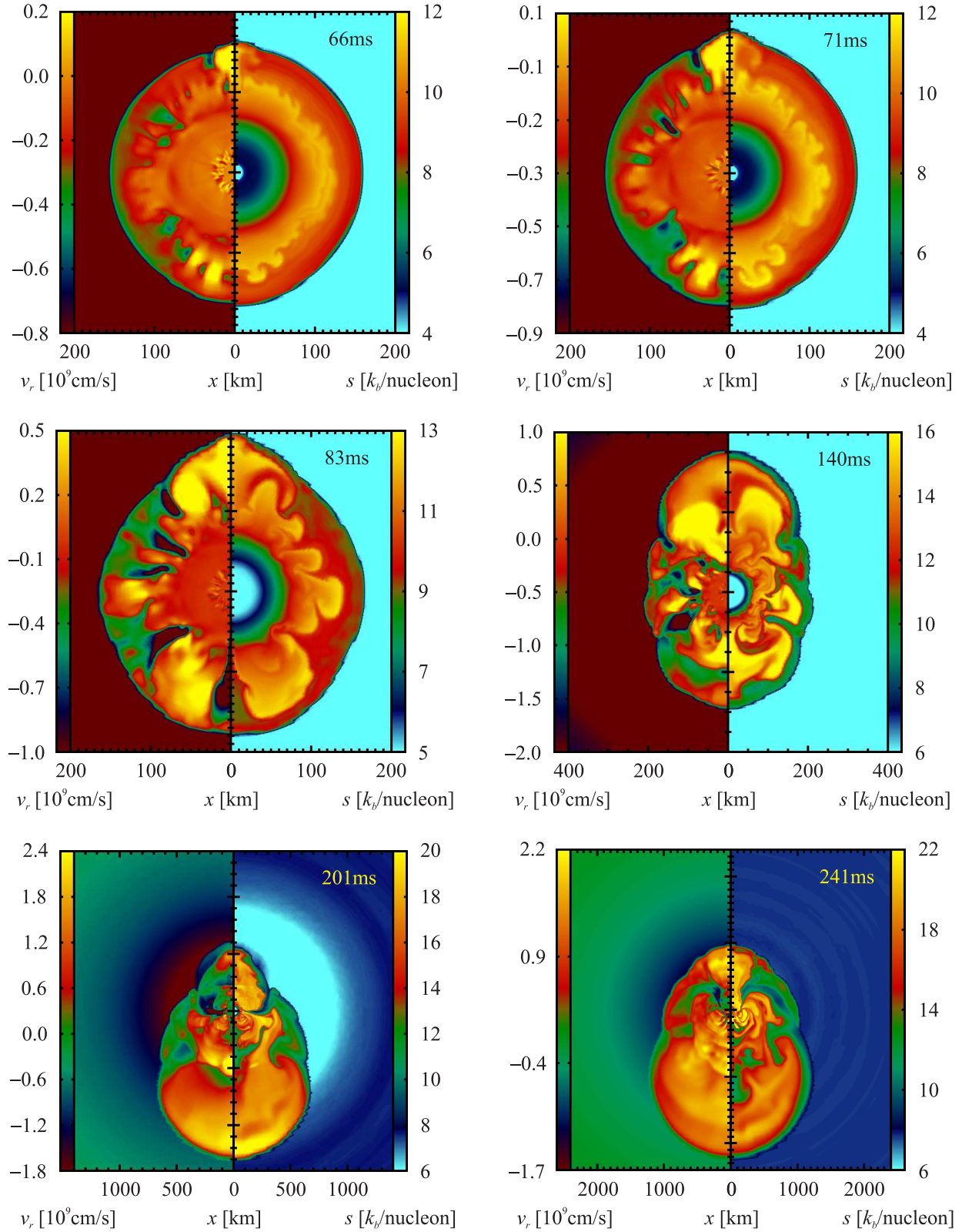


Figure 4. Snapshots of the evolution of model u8.1, depicting the radial velocity v_r (left half of panels) and the entropy per baryon s (right half of panels) 66 ms, 71 ms, 83 ms, 140 ms, 200 ms, and 241 ms after bounce (from top left to bottom right). Once the gain region becomes convectively unstable, small-scale plumes begin to grow (66 ms, 71 ms) and merge into somewhat larger structures on the scale of $10^\circ \dots 50^\circ$ (83 ms). As convection becomes more violent, the deformation of the shock becomes more pronounced (140 ms), and a dipolar asymmetry finally develops after the shock starts to accelerate outward (201 ms, 241 ms).

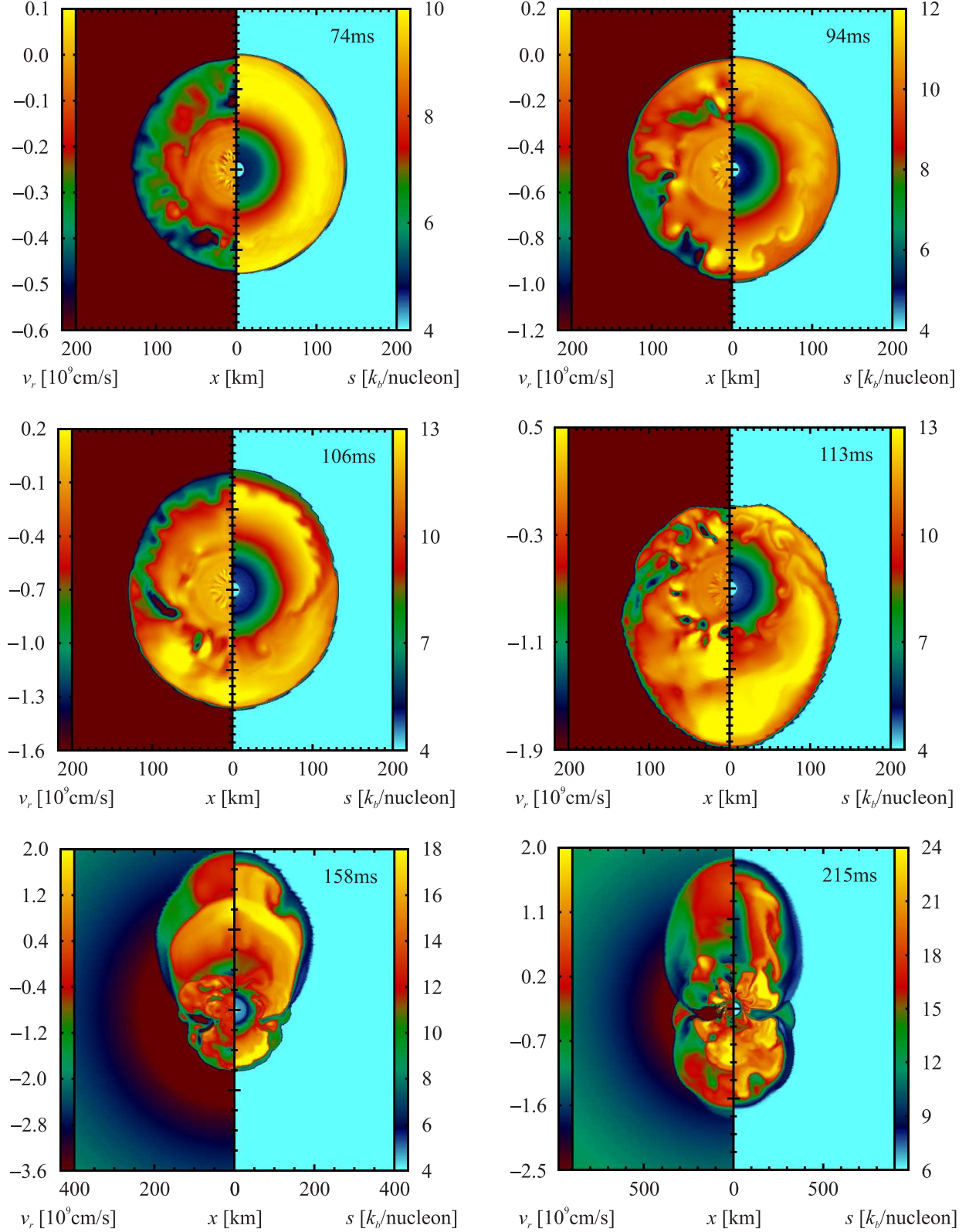


Figure 5. Snapshots of the evolution of model s27.0, depicting the radial velocity v_r (left half of panels) and the entropy per baryon s (right half of panels) 74 ms, 94 ms, 106 ms, 113 ms, 159 ms, and 215 ms after bounce (from top left to bottom right). The six panels exemplify the growth of the SASI in the linear regime (74 ms), the development of parasitic instabilities on top of a clear $\ell = 1$ asymmetry of the global entropy distribution (94 ms, 106 ms), the transition to the non-linear regime with the formation of a pronounced downflow (106 ms to 159 ms) and the phase of vigorous shock expansion (215 ms). Note the clearly different structure in the first four panels compared to the corresponding panels in Figure 4.

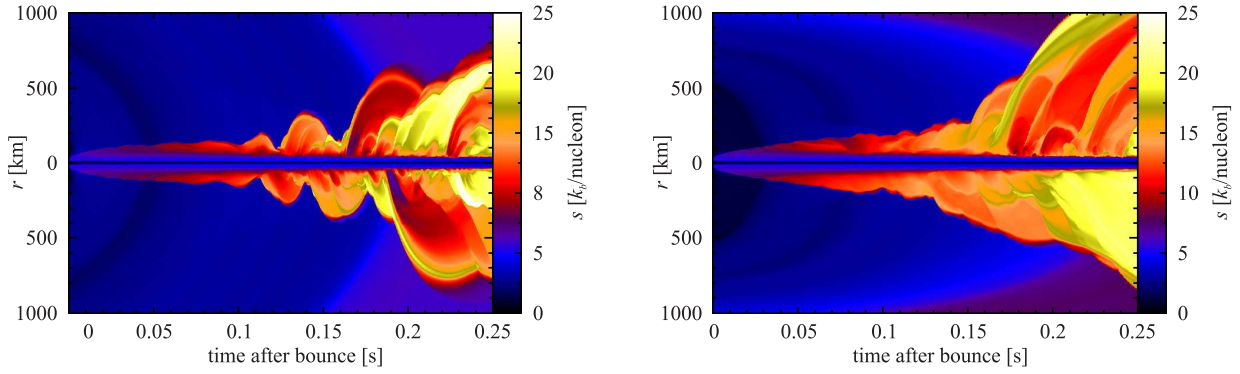


Figure 6. Entropy along the north and south polar axis as a function of time for models s27.0 (left) and u8.1 (right).

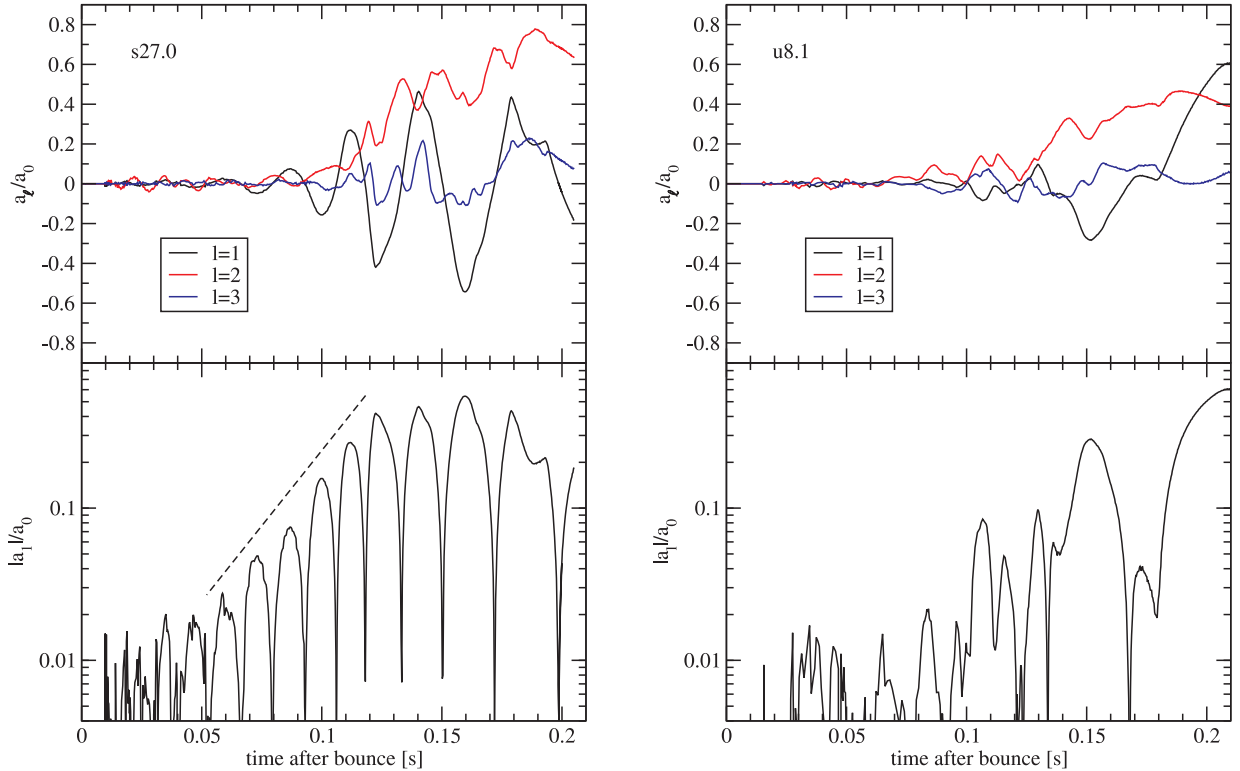


Figure 7. Coefficients for the decomposition of the shock surface into Legendre polynomials. The top panels show the first three normalized Legendre coefficients a_ℓ/a_0 for model s27.0 (left) and model u8.1 (right). In order to better exemplify the growth of the $\ell = 1$ mode, $|a_1|/a_0$ is also plotted on a logarithmic scale in the bottom panels. The dashed line roughly denotes the slope of the exponential growth of the SASI up to ~ 120 ms in model s27.0.

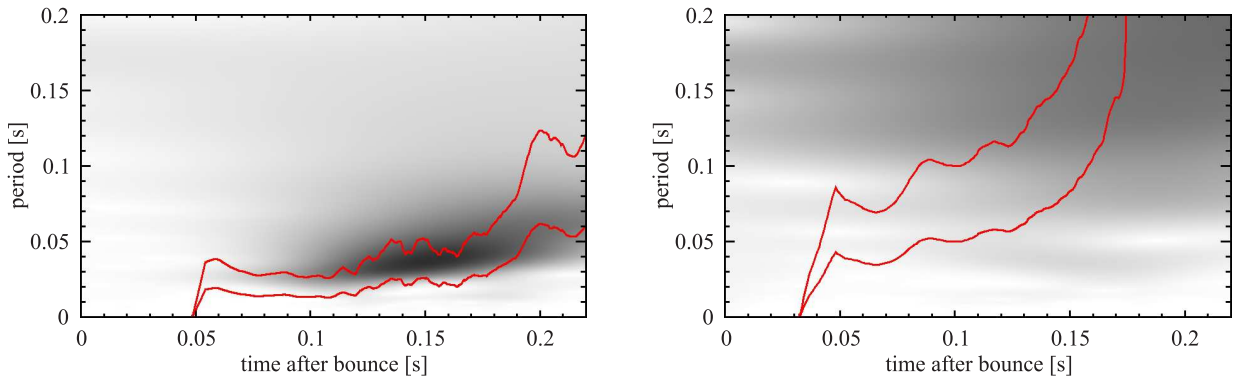


Figure 8. Wavelet spectrograms of the normalized Legendre coefficient a_1/a_0 of the $l = 1$ mode of the shock for model s27.0 (left) and model u8.1 (right). Large values of the wavelet transform are indicated by darker shades. The red curves roughly define a band in which an advective-acoustic instability should surface; the upper and lower curves show the (smoothed) time evolution of the advection time-scale τ_{adv} and of $2\tau_{\text{adv}}$, respectively.

comes quite dissimilar as soon as the gain region forms a few tens of milliseconds after bounce. Model u8.1 (Figure 4) conforms to the “standard” behavior exhibited by all recent first-principle explosion simulations (Marek & Janka 2009; Müller et al. 2012): The convective instability develops first, and perturbations at intermediate scales (corresponding to multipole orders of $\ell \gtrsim 5 \dots 10$) grow fastest, cf. Foglizzo et al. 2006, 2007). Larger plumes only form once convection has become vigorous and the shock has already expanded quite considerably (cp. the $11.2M_{\odot}$ case of Müller et al. 2012). A strong non-oscillatory dipolar shock deformation appears at late time once the explosion is underway, and this deformation seems to be driven by buoyant neutrino-heated plumes rather than by genuine SASI activity.

Model s27.0 behaves in a completely different manner (Figure 5). Here we first observe small, but clearly recognizable linear SASI oscillations (first panel of Figure 5). Later, as the amplitude of the SASI increases, parasitic Rayleigh-Taylor and Kelvin-Helmholtz instabilities grow on top of the SASI flow, but these remain localized, appearing and disappearing as the shock oscillates back and forth, and never growing into developed convection. The different character of the post-shock flow can also be seen in Figure 6, which shows the time-evolution of the entropy along the polar axis for both models and illustrates that – unlike model 8.1, s27.0 indeed exhibits the sloshing motions characteristic of the SASI. Until ~ 180 ms the expansion and contraction of the shock in the northern and southern hemispheres are nicely antisynchronized.

The velocity fluctuations in the gain region steadily grow in magnitude in model s27.0, eventually leading to the formation of secondary shocks (see the fifth panel of Figure 5). It is likely that these strong velocity fluctuations are responsible for pushing the shock further out because they provide an additional Reynolds stress contribution for the angle-averaged and time-averaged flow on top of the thermal pressure. Moreover, the thermal pressure itself is increased once dissipation in secondary shock starts to convert kinetic energy stored in the SASI motions into thermal energy. The dynamical importance of both these effects depends on the typical velocity δv of the aspherical flow perturbations, which determines the ratio of the Reynolds stresses $\rho \delta v^2$ and the kinetic energy to the thermal pressure P_{therm} and energy density $\rho \epsilon_{\text{therm}}$, respectively:

$$\rho \delta v^2 / P_{\text{therm}} \propto (1/2 \rho \delta v^2) / (\rho \epsilon_{\text{therm}}) \propto \delta v^2 / c_s^2 = \text{Ma}^2 \quad (1)$$

Once the SASI reaches the non-linear stage in model s27.0, the typical Mach number Ma (determined from angular root mean square averages of the lateral velocity component) exceeds $\gtrsim 0.5$ in large parts of the gain region and peaks at ~ 1 near the average shock radius, clearly indicating the dynamical importance of aspherical instabilities in that model. In that sense, model s27.0 may provide an example for SASI-driven shock expansion *prior* to the explosion as opposed to the neutrino-driven shock expansion that roughly sets in as $\tau_{\text{adv}}/\tau_{\text{heat}}$ exceeds unity.

We emphasize that these mechanisms for shock expansion are, of course, not specific to the SASI; indeed Murphy et al. (2012) demonstrated that the inclusion of the Reynolds stresses in the shock jump condi-

tions largely accounts for the increased shock radii in their convective models. However, while the immediate cause for the expansion of the shock is similar in model s27.0 to convectively-aided explosion models like u8.1 or those of Murphy et al. (2012), the ultimate source for the energy of aspherical motions is different: As long as the SASI remains the dominant instability, it essentially feeds directly on the kinetic energy of the accreted matter whereas convection is (indirectly) powered by neutrino heating.

3.2. Evidence for the SASI – Quantitative Analysis

For model s27, we thus have a SASI-like flow morphology reminiscent of simulations with no (Blondin et al. 2003) or suppressed (Scheck et al. 2008) neutrino heating. The associated aspherical velocities apparently become large enough (i.e. on the order of the speed of sound) to be dynamically relevant. But model s27 furnishes further evidence pointing to the SASI as the initially dominant instability besides the qualitative flow morphology.

A mode analysis of the shock surface, based on a decomposition into Legendre polynomials, confirms the dramatic differences in the growth of hydrodynamical instabilities (Figure 7). The expansion coefficients a_{ℓ} are given by

$$a_{\ell} = \frac{2\ell + 1}{2} \int_0^{\pi} r_{\text{sh}}(\theta) P_{\ell}(\cos \theta) \sin \theta \, d\theta, \quad (2)$$

and the first three coefficients a_1 , a_2 , and a_3 (normalized to the angle-averaged shock position $\langle r_{\text{sh}} \rangle = a_0$). The convectively-dominated model u8.1 (right panel of Figure 7) is characterized by relatively weak shock oscillations until ~ 130 ms when the explosive runaway due to neutrino heating is already underway. Afterwards, a pronounced dipole ($\ell = 1$) and quadrupole ($\ell = 2$) mode appear, but there is no trace of periodic oscillations at any stage. Apparently, the growth of the low- ℓ modes is a stochastic process driven by the convective plumes in this case. Later in the explosion, the geometry becomes more stable with a big buoyant bubble in the southern hemisphere. The dominance of such large-scale bubbles at late times is in agreement with analytic estimates for extended convective regions with a small, almost point-like heating source (Chandrasekhar 1961; Foglizzo et al. 2006).

By contrast, model s27.0 (left panel of Figure 7) exhibits shock oscillations with a well-defined periodicity for the $\ell = 1$ mode as expected for a relatively unperturbed SASI (cf. the numerical experiments by Scheck et al. 2008). The expected exponential growth of the dipole amplitude $|a_1|/a_0$ from ~ 0.02 to ~ 0.4 during the linear phase can be observed for several oscillation periods, and a growth rate $\omega_{\text{SASI}} \approx 45 \text{ s}^{-1}$ can be deduced. The quadrupole amplitude ($\ell = 2$) increases in a non-oscillatory manner after ~ 90 ms, which may be a result of the transition to the non-linear regime. Moreover, we expect the oscillation period to scale with the advection time-scale by a factor between unity and $\lesssim 2$ if an advective-acoustic cycle operates in model s27.0 (Foglizzo et al. 2007; Scheck et al. 2008; Guilet & Foglizzo 2012). This confirmed by a wavelet

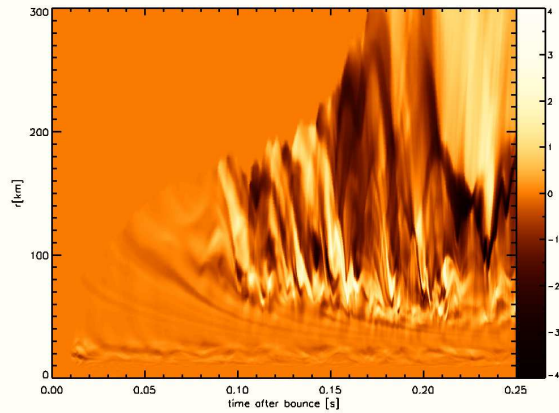
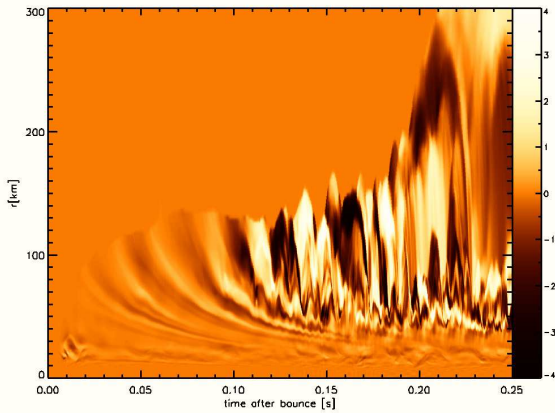


Figure 9. Lateral velocity v_θ in the equatorial plane as a function of time and radius for model s27.0 (left) and model u8.1 (right).

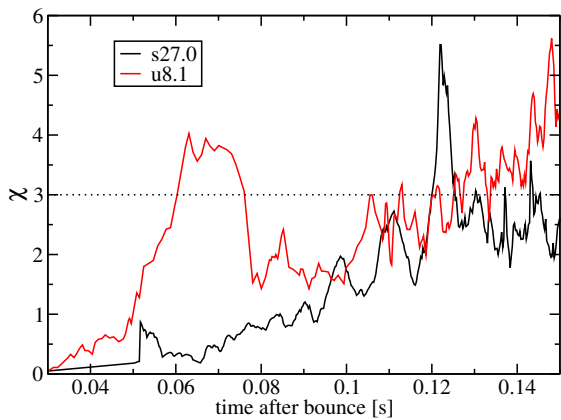


Figure 10. Evolution of the stability parameter χ for model s27.0 (black) and model u8.1 (red). The threshold value of $\chi \approx 3$ for convection is reached about 60 ms after bounce for model u8.1, whereas convective stability applies for s27.0 until 120 ms when the SASI has already grown to the non-linear regime. Note that χ becomes less meaningful as the post-shock flow develops strong asphericities. For this reason, e.g., the fact that χ drops below three at $t \approx 0.08$ s once convection has become vigorous does not indicate declining convective activity.

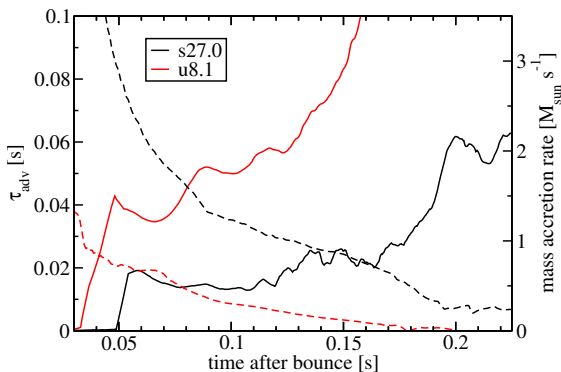


Figure 11. Advection time-scale τ_{adv} (solid lines) and mass accretion rate \dot{M} (dashed lines) for model s27.0 (black) and model u8.1 (red). The time-scales are evaluated as described in Müller et al. (2012), and the curves have been smoothed using a running average over 5 ms.

analysis of the $\ell = 1$ coefficient of the shock position using the Morlet wavelet (Torrence & Compo 1998) shown in Figure 8. Even after ~ 150 ms, when the underlying linear SASI eigenmode can no longer be easily discerned

in the post-shock flow (see the last two panels in Figure 5 and 4), the advection time-scale apparently still sets the oscillation period. This is in stark contrast to model u8.1, for which the wavelet spectrogram never shows a lot of power in the expected “SASI frequency band”. The antisynchronized variation of the shock radius along the north and south polar axis (left panel of Figure 6) that can be discerned until ~ 180 ms also points to a global low- ℓ instability; such a correlated variation of the shock radius in opposite directions is probably hard to reconcile with a stochastic forcing of low- ℓ modes by convection.

Up to ~ 150 ms, a closer look at the post-shock velocity field even reveals the advective part of the SASI amplification directly. Figure 9 clearly shows the advection of coherent perturbations in the lateral velocity (consistent with the $\ell = 1$ sloshing mode) from the shock to the deceleration region at the proto-neutron star surface for about 100 ms. Around ~ 150 ms, the perturbations become somewhat crinkled due to the action of parasitic instabilities, but a temporal quasi-periodicity can still be recognized. In model u8.1, we see only very faint traces of such coherent perturbations prior to the onset of convection.

There are thus good reasons for classifying model s27 as “SASI-dominated” and model u8.1 as “convection-dominated” at least for first ~ 150 ms. The late-time behavior around and after shock revival is probably more complicated in both cases. During this phase, neutrino heating evidently plays a major role for the dynamics and ultimately powers the explosion, and buoyancy-driven instabilities certainly become important in the process. However, this does not imply that steady-state convection alone furnishes an appropriate picture for the post-shock flow at this stage. The simulations rather suggest a complicated interplay between neutrino-heated, buoyancy-driven bubbles, internal shocks and acoustic waves, supersonic downflows, and an aspherical shock that creates large non-radial velocities in the post-shock region (bottom panels of Figures 4 and 5). The characterization of this phase will require a better understanding of the interaction of the different hydrodynamical instabilities in the fully non-linear phase.

3.3. Conditions for SASI-Dominated and Convectively-Dominated Flow

Why are the two models s27.0 and u8.1 dominated by different hydrodynamical instabilities, and why, in particular, is convection suppressed for the $27M_\odot$ progenitor despite neutrino heating in the gain layer? The key for understanding the differences is connected to the fact that the presence of a negative entropy gradient in the heating region is not sufficient for the onset of convection as pointed out by Foglizzo et al. (2006). Under the assumption of a stalled accretion shock, any convective perturbation is advected out of the gain layer within a finite time, and convection can develop only if the perturbation is amplified sufficiently within this time frame. Using a more rigorous mathematical analysis, Foglizzo et al. (2006) derived a growth parameter χ that is defined in terms of the Brunt-Väisälä frequency ω_{BV} and the spherically averaged advection velocity $\langle v_r \rangle$ as follows,

$$\chi = \int_{r_g}^{\langle r_{\text{sh}} \rangle} \frac{\text{Im } \omega_{\text{BV}}}{|\langle v_r \rangle|} dr, \quad (3)$$

where the integral runs from the gain radius r_g to the average shock radius r_{sh} . Note that only the region where $\omega_{\text{BV}}^2 < 0$ indicates *local* instability in the fluid frame contributes to the integral. Foglizzo et al. (2006) find a threshold condition of $\chi \gtrsim 3$ for convective instability in the gain region, which has been confirmed by parametrized as well as first-principle simulations (Buras et al. 2006a; Scheck et al. 2008; Fernández & Thompson 2009b). We emphasize that the criterion $\chi \gtrsim 3$ has been derived by Foglizzo et al. (2006) for the *linear* regime and may no longer be useful for determining the presence or absence of convective instability once significant non-spherical perturbations develop in the post-shock region.

The time evolution of χ for our two models is shown in Figure 10. Clearly, the parameter χ indicates that convection should set in at ~ 60 ms for u8.1, which is exactly what we observe (Figure 4). For s27.0, on the other hand, χ is very low at this junction, and only reaches the critical value $\chi = 3$ some 120 ms after bounce, when the flow is already strongly aspherical due to the activity of the SASI (Figure 7) and χ may no longer be a reliable measure for convective instability.

The conditions for effective SASI growth are quite different. Here, a short advection time-scale τ_{adv} is helpful: In the picture of the advective-acoustic cycle, the linear growth rate ω_{SASI} is given in terms of the cycle efficiency \mathcal{Q} and the duration τ_{cyc} of the cycle by

$$\omega_{\text{SASI}} = \frac{\ln |\mathcal{Q}|}{\tau_{\text{cyc}}}, \quad (4)$$

as shown by Foglizzo et al. (2006). A smaller shock stagnation radius and advection time-scale also imply a shorter cycle duration τ_{cyc} , and hence conditions favorable for a more rapid growth of the SASI.⁵ Since τ_{adv} is shorter by a factor of 2...4 in model s27.0 compared to u8.1 (Figure 11), considerably more vigorous SASI activity is to be expected. Moreover, convection could possibly destroy the coherence of the entropy, vorticity,

⁵ Qualitatively, the same dependence would be expected for a purely acoustic cycle. Whether the SASI grows due to advective-acoustic or purely acoustic feedback is therefore irrelevant for our discussion.

and acoustic waves involved in the amplification cycle (Guilet et al. 2010) even if it develops as a primary and not as a parasitic instability so that the very absence of convection for the $27M_\odot$ progenitor may also be a crucial factor for violent SASI activity.

Given these conditions, the predominance of the SASI and convection in model s27.0 and model u8.1, respectively, can be well accounted for, but the growth conditions can be further connected to the progenitor structure. The shorter advection time-scale in s27.0 is a direct result of a significantly higher accretion rate (by a factor of ~ 4 at 150 ms), which is in turn a direct consequence of the presence of a dense and rather massive silicon shell on top of the iron core (see, e.g., Woosley & Heger 2012 for the relation between the progenitor structure and the time-dependence of \dot{M}). The higher mass accretion rate leads to a smaller shock stagnation radius (Figure 2) after 30 ms post-bounce and thus to a more narrow post-shock layer as well as higher pre- and post-shock velocities, which implies a reduction of the accretion time-scale. Particularly at later stages, the stronger gravitational field of the proto-neutron star, whose baryonic mass reaches some $1.65M_\odot$ compared to $1.36M_\odot$ for u8.1 also contributes to the shorter advection time-scale. According to Equation (3), this will reduce the value of χ and therefore inhibit the development of convection.

Potentially, the larger advection velocities in the gain region could be compensated by a higher value of ω_{BV} in Equation (3), which might result from the stronger neutrino heating that may be expected because of an enhanced accretion luminosity (and hence stronger heating) in model s27.0. Larger neutrino luminosities and mean energies are indeed observed for model s27.0 (Figure 12), but what does this imply for the instabilities in the gain region?

To decide this question, we estimate the dependence of the unstable non-adiabatic gradient, e.g., of the internal energy density ϵ , on the neutrino emission and the heating efficiency by means of simple zeroth-order approximation for the solution of the internal energy equation for an infalling mass shell:

$$\left(\frac{\partial \epsilon}{\partial r} \right)_{\text{heating}} \propto \frac{\dot{q}_\nu \tau_{\text{adv}}}{r_{\text{sh}} - r_g} \propto \frac{\dot{Q}_\nu \tau_{\text{adv}}}{M_g (r_{\text{sh}} - r_g)} \propto \frac{\dot{Q}_\nu}{\dot{M} (r_{\text{sh}} - r_g)} \quad (5)$$

Here, \dot{q}_ν is the mass-specific neutrino heating rate, which is approximated in terms of the volume-integrated heating rate \dot{Q}_ν and the mass in the gain region $M_g \sim \dot{M} \tau_{\text{adv}}$. Equation (5) shows that stronger heating might be balanced by a larger \dot{M} , but as \dot{Q}_ν still depends on \dot{M} both through the post-shock stratification and the accretion luminosity Equation (5) does not help very much.

It is more useful to reformulate Equation (5) in terms of two efficiency parameters η_{heat} and η_{conv} for the neutrino heating and for the conversion of gravitational energy into electron (anti-)neutrinos. The familiar definition of the heating efficiency (Marek & Janka 2009; Müller et al. 2012) in terms of the volume-integrated heating rate \dot{Q}_{heat} in the gain region and the electron neutrino and antineutrino luminosities⁶ L_{ν_e} and $L_{\bar{\nu}_e}$,

⁶ We use the total angle-integrated neutrino energy flux measured at infinity (Figure 12) for L_{ν_e} and $L_{\bar{\nu}_e}$. Note that η_{heat} could be interpreted as an effective (non-Rosseland) frequency-averaged

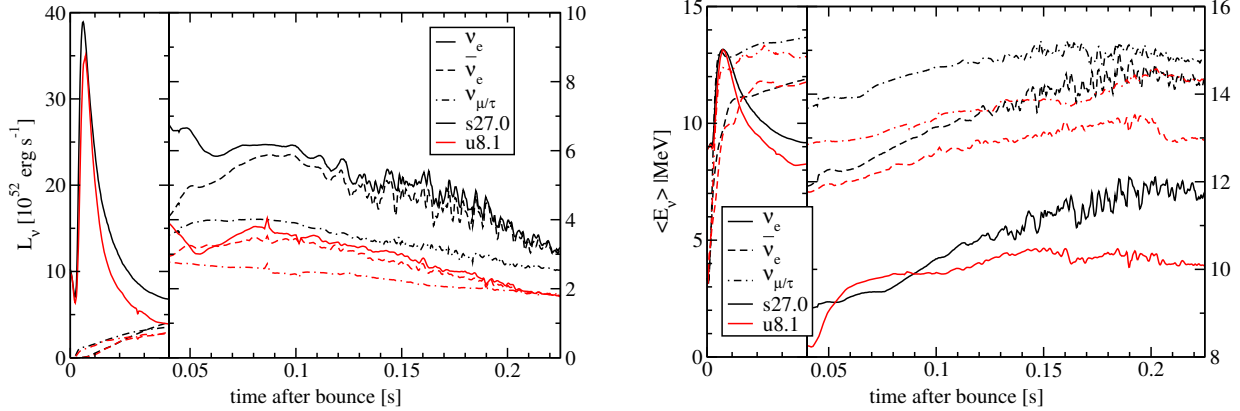


Figure 12. Neutrino luminosities (left panel) and mean energies (right panel) for s27.0 (black) and u8.1 (red). Solid, dashed, and dash-dotted lines are used for ν_e , $\bar{\nu}_e$, and $\nu_{\mu/\tau}$, respectively. Note that we plot angle-averaged quantities extracted at a fiducial observer radius of 400 km.

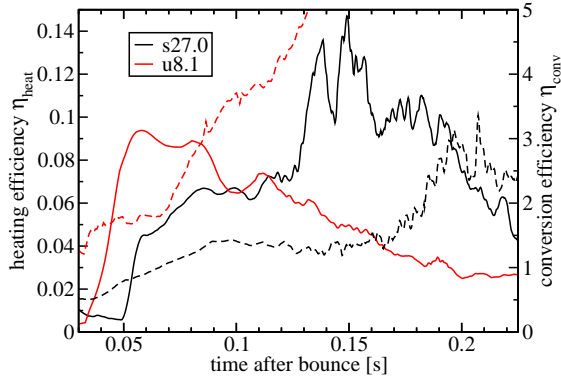


Figure 13. Heating efficiency η_{heat} (solid lines) and conversion efficiency η_{conv} (dashed lines) for s27.0 (black) and u8.1 (red). All curves have been smoothed using a running average over 5 ms.

reads

$$\eta_{\text{heat}} = \frac{\dot{Q}_\nu}{L_{\nu_e} + L_{\bar{\nu}_e}}. \quad (6)$$

As a measure for the efficiency of the conversion of gravitational energy of the accreted material into neutrinos we define η_{conv} in terms of L_{ν_e} , $L_{\bar{\nu}_e}$, and \dot{M} as

$$\eta_{\text{conv}} = \frac{(L_{\nu_e} + L_{\bar{\nu}_e}) R}{GM\dot{M}}. \quad (7)$$

Small values of $\eta_{\text{conv}} < 1$ indicate an inefficient conversion of gravitational energy into accretion luminosity due to the fast advection of the accreted material through the cooling layer, whereas $\eta_{\text{conv}} > 1$ indicates an effective conversion and an additional enhancement of the electron (anti-)neutrino luminosity due to the diffusive neutrino flux from the deeper layers of the proto-neutron star. The unstable gradient manifestly depends on those two efficiencies:

$$\left(\frac{\partial \epsilon}{\partial r}\right)_{\text{heating}} \propto \frac{GM\eta_{\text{heat}}\eta_{\text{conv}}}{R(r_{\text{sh}} - r_{\text{g}})}. \quad (8)$$

As shown in Figure 13, both η_{heat} and η_{conv} remain significantly smaller for s27.0 than for u8.1 before the SASI starts to push the shock outwards at ~ 120 ms. The smaller heating efficiency η_{heat} in s27.0 at early times is a direct consequence of the rapid advection of material

optical depth of the gain region.

through the gain layer (Figure 11), which is compensated by a larger mass in the gain region at later times. Particularly large differences are observed for η_{conv} , which is larger by a factor of 2...4 in model u8.1 prior to the explosion and is therefore by far the most relevant term in Equation (8). At early times, the rapid post-shock advection in model s27.0 also results in somewhat inefficient cooling, whereas neutrino diffusion from the deeper regions of the proto-neutron star starts to enhance the electron (anti-)neutrino luminosity rather early for the $8.1M_\odot$ star and soon outweighs the accretion luminosity. As a consequence, the relative difference in luminosity between the two models (Figure 12) is much smaller than the relative difference of the accretion rates (Figure 11). The two terms in Equation (8) that could enhance the unstable gradient in s27.0 compared to u8.1 are the difference of the shock and gain radius in the denominator and the compactness parameter M/R . However, the effect of the different value for $r_{\text{sh}} - r_{\text{g}}$ is more than compensated for by different domain of integration in Equation (3) for the parameter χ , and the compactness M/R is only higher by $\sim 25\%$.

Our analysis thus provides the clue for understanding why the larger luminosities in model s27.0 are not helpful for fostering the growth of convective instabilities: The decisive quantity is the ratio between the luminosity and a fiducial accretion luminosity $GM\dot{M}/R$ (rather than the luminosity itself), and a high accretion rate will decrease rather than increase this “conversion efficiency”.

4. DISCUSSION AND CONCLUSIONS

We presented new two-dimensional general relativistic explosion models for a metal-poor $8.1M_\odot$ and solar-metallicity $27M_\odot$ progenitor. Our successful explosion models for these stars exemplify two possible regimes for the growth of hydrodynamic instabilities in core-collapse supernovae. While the $8.1M_\odot$ star conforms to the familiar picture of neutrino-driven convection growing first and giving rise to low- ℓ shock oscillations afterwards as shock expansion sets in (see, e.g., the $11.2M_\odot$ and $15M_\odot$ models of Marek & Janka 2009 and Müller et al. 2012), the SASI is the primary instability for the $27M_\odot$ progenitor. In this model, we can clearly identify the SASI and its characteristic features during the linear growth phase, and find that the flow remains distinctively differ-

ent from the convective $8.1M_{\odot}$ model in the non-linear regime. This ‘‘SASI-dominated’’ regime is observed here for the first time in a fully self-consistent neutrino transport simulation; the purely hydrodynamical models of Blondin et al. (2003), in which the SASI was initially discovered, and the SASI models of Scheck et al. (2008), which relied on a fast contraction of the proto-neutron star, may thus capture the dynamics in the supernova core better than recently suggested (Burrows et al. 2012; Murphy et al. 2012). *Whether convection or the SASI emerges as the dominant instability evidently depends on the conditions in the accretion flow onto the proto-neutron star.* Moreover, the SASI plays a major role during the evolution of the $27M_{\odot}$ progenitor towards an explosion as it already pushes the shock out to an average radius of 300 km before the runaway condition for neutrino-driven shock expansion is finally reached and parasitic convective activity becomes very strong. It is noteworthy that, contrary to the expectations of Fryer et al. (2012) and Belczynski et al. (2011), such a SASI-aided explosion can be initiated at a similarly early stage as in the convectively-dominated model u8.1, i.e. less than 200 ms after bounce.

There may be a number of conspiring factors that allow the $27M_{\odot}$ progenitor to reach the SASI-driven regime: Any effect that leads to higher post-shock advection velocities could potentially decide about the character of the dominant aspherical instability in the pre-explosion phase. For our $27M_{\odot}$ model, the following differences to other recent two-dimensional first-principle simulations of supernova explosions (Buras et al. 2006a; Marek & Janka 2009; Bruenn et al. 2009; Suwa et al. 2010; Muller et al. 2012) as well as convective models based on a simple light-bulb approximation (Murphy & Burrows 2008; Nordhaus et al. 2010b; Hanke et al. 2011; Burrows et al. 2012; Murphy et al. 2012) contribute – certainly to varying degrees – to the short advection time-scale:

1. The iron core of the progenitor – and hence the proto-neutron star – is fairly massive, and is surrounded by a thick and rather dense silicon shell. The mass accretion rate therefore remains high long after the gain region has formed. This implies a small shock stagnation radius and a short advection time-scale, which in turn suppresses convective activity (see Equation 3). On the other hand, the short advection time-scale is conducive to efficient SASI growth (see Equation 4).
2. General relativity further contributes to the short advection time-scale as it leads to a more compact neutron star (Bruenn et al. 2001; Muller et al. 2012; Lentz et al. 2012), an effect that is all the more important as the proto-neutron star is already quite massive to begin with. Newtonian models could thus systematically miss the SASI-driven regime.
3. The nuclear EoS LS220 produces fairly compact neutron stars in agreement with recent radius estimates (Steiner et al. 2010; Hebeler et al. 2010), again contributing to fast advection through the gain layer (cp. Marek & Janka 2009 for the dependence of the accretion shock radius on the

EoS). SASI growth may be inhibited in simulations (Burrows et al. 2006; Murphy & Burrows 2008; Burrows et al. 2012; Murphy et al. 2012) using the Shen EoS (Shen et al. 1998) with its high value for the symmetry energy of 36.9 MeV.

4. Including the full neutrino transport for all flavors allows the proto-neutron star to contract properly, whereas light-bulb models and simulations neglecting μ and τ neutrinos may suppress or underestimate the contraction (and hence the advection velocities) considerably. Light-bulb models that disregard neutrino diffusion from the neutron star interior neglect this aspect of proto-neutron star evolution completely.

With all these elements working in tandem to decrease the accretion shock radius prior to the onset of multi-dimensional instabilities, the competition between buoyancy effects and post-shock advection is heavily tilted towards the latter, resulting in a suppression of convection (Foglizzo et al. 2006), while the growth of the SASI is accelerated. The individual contribution of each factor, as well as certain balancing effects due to enhanced electron neutrino and antineutrino luminosities and spectra, would obviously merit further investigation, and cannot be quantified based on a single model.

The realization that the SASI rather than convection can be the primary instability under certain conditions encountered in self-consistent 2D supernova simulations opens up several interesting perspectives: Can a model that is initially dominated by convection perhaps undergo a late-time transition to the SASI-dominated regime if the shock retracts sufficiently far? This could, for example, provide an explanation for the late explosions of a $15M_{\odot}$ star of Marek & Janka (2009) and Muller et al. (2012), which are associated with strong shock oscillations. Furthermore, the growth and saturation behavior of the SASI in 3D become a major issues: Could the parasitic instabilities that have been proposed as saturation mechanism (Guilet et al. 2010) be sufficiently suppressed to allow vigorous SASI activity in 3D as well? Could even a partial suppression due to fast advection explain the development of low- ℓ modes, which may be inhibited under other circumstances because of the forward turbulent cascade in 3D (Hanke et al. 2011)? Will the $\ell = 1$ sloshing mode be replaced by a spiral mode that might spin up the neutron star (Blondin & Mezzacappa 2007; Fernandez 2010) much more effectively than suggested by recent simulations (Wongwathanarat et al. 2010; Rantsiou et al. 2011)? Will the SASI saturate at lower amplitudes in 3D as the kinetic energy is shared among a larger number of modes as suggested by Iwakami et al. (2009), or will the kinetic energy contained in non-radial motions even become larger as more modes can be excited? Will the growth and saturation depend on the initial seed perturbations and the rotation rate of the progenitor? All these questions will need to be answered *not only for restricted parametrized setups*, but for the realistic conditions actually encountered in self-consistent neutrino hydrodynamics simulations of a large variety of progenitors. The future exploration of the SASI and convection will also require better methods for discriminating between these

two – possibly sometimes co-existing – instabilities in the non-linear regime. The role of SASI and convection in core-collapse supernovae as well as their mutual interaction are thus bound to remain fruitful topics in supernova physics.

AH thanks Candace Joggerst and Stan Woosley for help with the progenitor star models. This work was supported by the Deutsche Forschungsgemeinschaft through the Transregional Collaborative Research Center “Gravitational Wave Astronomy” and the Cluster of Excellence EXC 153 “Origin and Structure of the Universe” (<http://www.universe-cluster.de>). AH has been supported, in part, by the DOE Program for Scientific Discovery through Advanced Computing (SciDAC; DE-FC02-09ER41618), by the US Department of Energy under grant DE-FG02-87ER40328, by NSF grant AST-1109394, by a Larkin’s Fellowship from Monash University, and by ARC through Future Fellowship ID FT120100363. The computations were performed on the IBM p690 of the Computer Center Garching (RZG), on the Curie supercomputer of the Grand Equipement National de Calcul Intensif (GENCI) under PRACE grant RA0796, on the Cray XE6 and the NEC SX-8 at the HLRS in Stuttgart (within project SuperN), on the JU-ROPA systems at the John von Neumann Institute for Computing (NIC) in Jülich, and on the Itasca Cluster of the Minnesota Supercomputing Institute.

REFERENCES

- Arnett, W. D., Bahcall, J. N., Kirshner, R. P., & Woosley, S. E. 1989, *ARA&A*, 27, 629
- Belczynski, K., Wiktorowicz, G., Fryer, C., Holz, D., & Kalogera, V. 2011, *ArXiv e-prints*, 1110.1635
- Bethe, H. A. 1990, *Rev. Mod. Phys.*, 62, 801
- Blondin, J. M., & Mezzacappa, A. 2006, *ApJ*, 642, 401
- . 2007, *Nature*, 445, 58
- Blondin, J. M., Mezzacappa, A., & DeMarino, C. 2003, *ApJ*, 584, 971
- Bruenn, S. W., De Nisco, K. R., & Mezzacappa, A. 2001, *ApJ*, 560, 326
- Bruenn, S. W., Dirk, C. J., Mezzacappa, A., Hayes, J. C., Blondin, J. M., Hix, W. R., & Messer, O. E. B. 2006, *J. Phys. Conf. Ser.*, 46, 393
- Bruenn, S. W., Mezzacappa, A., Hix, W. R., Blondin, J. M., Marronetti, P., Messer, O. E. B., Dirk, C. J., & Yoshida, S. 2009, *Journal of Physics Conference Series*, 180, 012018
- Buras, R., Janka, H.-T., Rampp, M., & Kifonidis, K. 2006a, *A&A*, 457, 281
- Buras, R., Rampp, M., Janka, H.-T., & Kifonidis, K. 2006b, *A&A*, 447, 1049
- Burrows, A., Dolence, J. C., & Murphy, J. W. 2012, *ArXiv e-prints*, 1204.3088
- Burrows, A., & Fryxell, B. A. 1992, *Science*, 258, 430
- Burrows, A., & Hayes, J. 1996, *Physical Review Letters*, 76, 352
- Burrows, A., Hayes, J., & Fryxell, B. A. 1995, *ApJ*, 450, 830
- Burrows, A., Livne, E., Dessart, L., Ott, C. D., & Murphy, J. 2006, *ApJ*, 640, 878
- Chandrasekhar, S. 1961, *Hydrodynamic and Hydromagnetic Stability* (Oxford: Clarendon)
- Cordero-Carrión, I., Cerdá-Durán, P., Dimmelmeier, H., Jaramillo, J. L., Novak, J., &ourgoulhon, E. 2009, *Phys. Rev. D*, 79, 024017
- Demorest, P. B., Pennucci, T., Ransom, S. M., Roberts, M. S. E., & Hessels, J. W. T. 2010, *Nature*, 467, 1081
- Fernández, R. 2010, *ApJ*, 725, 1563
- . 2012, *ApJ*, 749, 142
- Fernández, R., & Thompson, C. 2009a, *ApJ*, 703, 1464
- . 2009b, *ApJ*, 697, 1827
- Foglizzo, T. 2002, *A&A*, 392, 353
- Foglizzo, T., Galletti, P., Scheck, L., & Janka, H.-T. 2007, *ApJ*, 654, 1006
- Foglizzo, T., Scheck, L., & Janka, H.-T. 2006, *ApJ*, 652, 1436
- Fryer, C. L., Belczynski, K., Wiktorowicz, G., Dominik, M., Kalogera, V., & Holz, D. E. 2012, *ApJ*, 749, 91
- Fryer, C. L., & Warren, M. S. 2002, *ApJ*, 574, L65
- Gawryszczak, A., Guzman, J., Plewa, T., & Kifonidis, K. 2010, *A&A*, 521, A38
- Guilet, J., & Foglizzo, T. 2012, *MNRAS*, 421, 546
- Guilet, J., Sato, J., & Foglizzo, T. 2010, *ApJ*, 713, 1350
- Hammer, N. J., Janka, H., & Müller, E. 2010, *ApJ*, 714, 1371
- Hanke, F., Marek, A., Mueller, B., & Janka, H.-T. 2011, *ArXiv e-prints*, 1108.4355
- Hebeler, K., Lattimer, J. M., Pethick, C. J., & Schwenk, A. 2010, *Physical Review Letters*, 105, 161102
- Heger, A., Woosley, S. E., Zhang, W., & Joggerst, C. C. 2012, *ApJ*, in preparation
- Herant, M. 1995, *Phys. Rep.*, 256, 117
- Herant, M., Benz, W., & Colgate, S. 1992, *ApJ*, 395, 642
- Herant, M., Benz, W., Hix, W. R., Fryer, C. L., & Colgate, S. A. 1994, *ApJ*, 435, 339
- Iwakami, W., Kotake, K., Ohnishi, N., Yamada, S., & Sawada, K. 2008, *ApJ*, 678, 1207
- . 2009, *ApJ*, 700, 232
- Janka, H.-T. 2001, *A&A*, 368, 527
- Janka, H.-T., & Müller, E. 1994, *A&A*, 290, 496
- . 1996, *A&A*, 306, 167
- Kifonidis, K., Plewa, T., Janka, H.-T., & Müller, E. 2003, *A&A*, 408, 621
- Kifonidis, K., Plewa, T., Scheck, L., Janka, H.-T., & Müller, E. 2006, *A&A*, 453, 661
- Laming, J. M. 2007, *ApJ*, 659, 1449
- Lattimer, J. M., & Swesty, F. D. 1991, *Nucl. Phys. A*, 535, 331
- Lentz, E. J., Mezzacappa, A., Bronson Messer, O. E., Liebendörfer, M., Hix, W. R., & Bruenn, S. W. 2012, *ApJ*, 747, 73
- Marek, A., & Janka, H. 2009, *ApJ*, 694, 664
- Müller, B., Janka, H., & Dimmelmeier, H. 2010, *ApJS*, 189, 104
- Müller, B., Janka, H.-T., & Marek, A. 2012, *ArXiv e-prints*, 1202.0815
- Müller, E., & Janka, H.-T. 1997, *A&A*, 317, 140
- Murphy, J. W., & Burrows, A. 2008, *ApJ*, 688, 1159
- Murphy, J. W., Dolence, J. C., & Burrows, A. 2012, *ArXiv e-prints*, 1205.3491
- Nordhaus, J., Brandt, T. D., Burrows, A., & Almgren, A. 2012, *MNRAS*, 2901
- Nordhaus, J., Brandt, T. D., Burrows, A., Livne, E., & Ott, C. D. 2010a, *Phys. Rev. D*, 82, 103016
- Nordhaus, J., Burrows, A., Almgren, A., & Bell, J. 2010b, *ApJ*, 720, 694
- Ohnishi, N., Kotake, K., & Yamada, S. 2006, *ApJ*, 641, 1018
- Rampp, M., & Janka, H.-T. 2002, *A&A*, 396, 361
- Rantsiou, E., Burrows, A., Nordhaus, J., & Almgren, A. 2011, *ApJ*, 732, 57
- Scheck, L., Janka, H.-T., Foglizzo, T., & Kifonidis, K. 2008, *A&A*, 477, 931
- Scheck, L., Kifonidis, K., Janka, H.-T., & Müller, E. 2006, *A&A*, 457, 963
- Scheck, L., Plewa, T., Janka, H.-T., Kifonidis, K., & Müller, E. 2004, *Physical Review Letters*, 92, 011103
- Shen, H., Toki, H., Oyamatsu, K., & Sumiyoshi, K. 1998, *Nucl. Phys. A*, 637, 435
- Steiner, A. W., Lattimer, J. M., & Brown, E. F. 2010, *ApJ*, 722, 33
- Suwa, Y., Kotake, K., Takiwaki, T., Whitehouse, S. C., Liebendörfer, M., & Sato, K. 2010, *PASJ*, 62, L49+
- Swesty, F. D., Lattimer, J. M., & Myra, E. S. 1994, *ApJ*, 425, 195
- Takiwaki, T., Kotake, K., & Suwa, Y. 2012, *ApJ*, 749, 98, 1108.3989
- Thompson, T. A., Burrows, A., & Pinto, P. A. 2003, *ApJ*, 592, 434
- Thompson, T. A., Quataert, E., & Burrows, A. 2005, *ApJ*, 620, 861
- Torrence, C., & Compo, G. P. 1998, *Bulletin of the American Meteorological Society*, 79, 61
- Wongwathanarat, A., Janka, H., & Müller, E. 2010, *ApJ*, 725, L106
- Woosley, S. E., & Heger, A. 2012, *ApJ*, 752, 32
- Woosley, S. E., Heger, A., & Weaver, T. A. 2002, *Rev. Mod. Phys.*, 74, 1015
- Woosley, S. E., & Weaver, T. A. 1995, *ApJS*, 101, 181
- Yamasaki, T., & Yamada, S. 2007, *ApJ*, 656, 1019